Received: 13 July 2023 | Revised: 24 January 2024 | Accepted: 19 March 2024

DOI: 10.1002/pip.3802

SPECIAL ISSUE ARTICLE

PROGRESS IN PHOTOVOLTAICS WILEY

Optical design and bandgap engineering in ultrathin multiple quantum well solar cell featuring photonic nanocavity

Hosni Meddeb | **Kai Gehrke** | **Martin Vehse**

German Aerospace Center (DLR), Institute of Networked Energy Systems, Urban and Residential Technologies, Carl-von-Ossietzky-Str. 15, Oldenburg, 26129, Germany

Correspondence
Hosni Meddeb, German Aerospace Center (DLR), Institute of Networked Energy Systems, Urban and Residential Technologies, Carl-von-Ossietzky-Str. 15, 26129 Oldenburg, Germany.
Email: hosni.meddeb@dlr.de

Funding information
German Aerospace Center

Abstract

Ultrathin solar cells are efficient and captivating devices with unique technological and scientific features in terms of minimal material consumption, fast fabrication processes, and good compatibility with semi-transparent applications. Such photovoltaic (PV) technologies can enable effective synergy between optical and electronic confinements with large tuning capabilities of all the optoelectronic characteristics. In this work, the implications of the optical design and the bandgap engineering in ultrathin hydrogenated amorphous Si/Ge multiple quantum well (MQW) solar cells featuring photonic nanocavity are analyzed based on experimental measurements and optoelectronic modelling. By changing the period thicknesses and the positions of QWs inside the deep-subwavelength nanophotonic resonator, the spatial and spectral distributions of the optical field and the local absorption are strongly affected. This leads to a modulation of the absorption resonance condition, the absorption edge and the resulting photocurrent outputs. Because of quantum confinement effect, the change of MQW configurations with different individual QW periods while keeping similar total thickness of about 20 nm alters both the bandgap energy and the band offset at the QW/barrier heterojunctions. This in turn controls the photovoltage as well as the carrier collection efficiency in solar cells. The highest open circuit voltage and fill factor values are achieved by employing MQW device configuration with 2.5 nm-thin QWs. A record efficiency above 5.5% is reached for such emerging ultrathin Si/Ge MQW solar cell technology using thinner QWs with sufficient number, because of the optimum trade-off between all the optoelectronic characteristic outputs. The presented design rules for opaque ultrathin solar cells with quantum-confined nanostructures integrated in a photonic nanocavity can be generalized for the engineering of relevant multifunctional semitransparent PV devices.

1 | INTRODUCTION

Ultrathin solar cells feature reduced nanoabsorber thicknesses by orders of magnitude relative to conventional photovoltaic (PV) technologies.[1,2] Apart from the benefits in terms of materials consumption and cost savings, such ultrathin-film PV technologies can corroborate excellent compatibility with the diverse applications of integrated PV.[1,3–5] To enable tremendous thickness reduction while retaining high power conversion efficiency, several characteristics are desired with regard to the optical and electronic properties of absorbers and the architecture of PV devices.[1,2,5] Mainly, efficient ultrathin solar cells require a combination of photoactive materials with high absorption coefficients, light-trapping structures for the enhancement of light path and effective approaches for the collection of charge carriers.[1]

Regarding the optical aspect, different light management schemes such as Lambertian scattering and multi-resonant absorption are employed to preserve high values of photogenerated currents in thinner solar cells.[1] Among these concepts, optical nanocavities or nanophotonic resonators have been successfully implemented in various organic and inorganic thin-film PV technologies to enhance the light absorption because of multiple passes and strong interference effects.[1,6–13] In particular, "asymmetric Fabry-Perot (F-P)" nanophotonic cavities with highly lossy layers on reflecting surfaces allow strong optical confinement into narrow spatial dimensions with thicknesses significantly smaller than the incident optical wavelength.[14–19]

Regarding the electronic aspect, the thickness reduction in low-dimensional semiconductors (smaller than the fundamental De Broglie wavelength/exciton Bohr radius) induces a restriction in the spatial degrees of freedom for charge carriers.[20–22] Such quantum confinement (QC) effect leads to size-dependent changes in the optoelectronic properties of absorber materials.[23–25] Quantum-confined nanostructures have been widely developed in emerging high-efficiency PV technologies.[26,27] Especially, quantum well (QW) solar cells were realized using various semiconductor material systems.[28–32] These technologies can afford distinguished advantages including the ability of bandgap engineering, the alleviation of radiative recombination, the exploitation of excitonic absorption and the improvement of photocurrent with minimized voltage losses.[28,33,34]

Interestingly, the development of novel absorber materials and device architectures for PV devices can provide effective synergy between optical and electronic confinements in ultrathin PV technologies. In this context, these characteristics can be exceptionally satisfied by ultrathin QW solar cell with intrinsic nanoabsorber in the range of only 20 nm, based on hydrogenated amorphous silicon (a-Si:H) and germanium (a-Ge:H) nanostructures integrated in subwavelength photonic nanocavity.[21,23,35] In such structure, a-Ge:H layers with high absorption coefficient and significant QC susceptibility can fulfill the role of both nanoabsorber and quantum well.[21,23,35] Furthermore, a-Si:H/a-Ge:H heterojunction with good interface quality, suitable band offset for electronic transport and comparable refractive indices can form both QW/barrier heterostructures and lossy media in absorbing nanocavity.[21,35] However, the introduction of multiple quantum wells (MQW) architecture as nanoabsorber enables extra degree of freedom in the optical design for the optimization of the photocurrent and in the bandgap engineering for the enhancement of the electronic transport.[32,35] Considering the distinctiveness of the photoactive material system and the device concept, a thorough analysis of optical design and bandgap engineering capabilities in ultrathin amorphous Si/Ge MQW solar cells integrated in a nanophotonic cavity is still lacking.

In this work, the influence of different Si/Ge MQW nanoabsorber configurations on the characteristics of ultrathin solar cells featuring a deep-subwavelength photonic resonator is studied for the first time. This could be achieved by designing multiple nanoabsorber regions with different positions and period thicknesses inside the subwavelength absorbing nanocavity. By adopting the MQW configuration with thinner QW and specific number inside the absorbing nanocavity with highly reflective Ag mirror, the efficiency is improved above 5.5%, because of the optimum trade-off between all the optoelectronic characteristic outputs of the corresponding solar cell device. A detailed optoelectronic modelling analysis is conducted to gain further understanding of optical design and bandgap engineering principles. With changing the MQW configuration in the absorbing nanocavity, the absorption resonance and absorption edge conditions are altered. The photocurrent output is strongly controlled by the difference in spatial and spectral distributions of the optical field and the local absorption. Because of quantum-size effects, the sequential carrier transport and collection are affected by the change in bandgap energy and QW/barrier heterojunction discontinuity. This in turn controls the electronic characteristic parameters of PV devices. The established design rules for opaque ultrathin Si/Ge MQW solar cells are essential for the optimization of relevant multifunctional semi-transparent PV devices. Similar considerations for nanoabsorber architecture engineering should be adopted when opaque reflective back mirror is replaced by different semi-transparent conductive contacts such as switchable[36–38] or ultrathin metal electrodes[35] for window applications and with metal/oxide multilayers electrode in spectrally selective solar cell for greenhouse applications.[5,39] For semi-transparent ultrathin Si/Ge MQW devices, further investigations focusing on the effects of QWs number, barrier thickness and back reflector thickness will be insightful to achieve an optimum trade-off between efficiency and transparency.

2 | EXPERIMENTAL METHODS

On commercial glass substrates from Solayer GmbH (size: 10 × 10 cm^2), the front contacts were formed by 1 μm-thick films of Aluminum-doped Zinc Oxide ZnO:Al (AZO) having surface roughness RMS of about 15 nm. Prior the depositions, the samples underwent two-step solvent cleaning (acetone followed by isopropanol) in ultrasonic bath for 15 min each, rinsed in deionized water, and then, dried with N_2 gun. The solar cell structures consisted of hydrogenated amorphous silicon and germanium multilayers with n-i-p superstrate configuration as (n-a-Si:H/i-a-Si:H/ MQW /i-a-Si:H/p-a-Si:H) with thicknesses of (7 nm/3 nm /MQW/3 nm/7 nm). The transport layers for electrons (ETL) and for holes (HTL) as well as the buffer passivation layers on both sides forming the outer n/i and i/p regions were kept similar for all solar cell devices.

In the intrinsic MQW region, the alternation between i-a-Si:H quantum barrier (QB) and i-a-Ge:H quantum well (QW) layers was changed to obtain different periodic stratified architectures, while keeping similar total thickness for i-a-Ge:H material in the range of 20 nm. By varying the deposition duration of i-a-Ge:H layers, different QW thicknesses L_{QW} were obtained, as mentioned in Table S1.

Therefore, the following combinations of QW thicknesses and numbers are adopted: (2 × 10 nm), (3 × 6.7 nm), (4 × 5 nm), (5 × 4 nm), (8 × 2.5 nm). A gradient-bandgap MQW structure with gradual increase of QW thickness (2.5 nm/4 nm /5 nm/7.5 nm) from the front to the back of the device was also fabricated. The thicknesses of i-a-Si:H layers as QB interlayers separating for all MQW configurations were kept constant with L_{QB} of 1 nm. After the front contact opening through the glass substrate by laser scribing in microSTRUCTvario system from 3DMicromac, 200 nm-thick silver (Ag) layers were deposited through shadow mask. as reflective back contacts to define cell core areas of 1 × 1 cm^2. For the fabrication of solar cell devices, DC magnetron sputtering technique was used for the front and back electrodes deposition in Singulus Vistaris 600 system, whereas low-temperature Plasma Enhanced Chemical Vapor Deposition (PECVD) method at 13.56 MHz was employed for the coating of semiconductor functional layers in the cluster tool Von Ardenne CS-400P.

Ellipsometry measurements of single i-a-Ge:H layers with different thicknesses on glass were conducted in SENTECHSE850-ST system for the determination of optical bandgaps. Then, the computation of refractive indices were done using SpectraRay software included in the ellipsometry software package for data modelling and fitting. Optical spectra measurements were performed by means of UV–VIS spectrophotometry in Cary 5,000 instrument from Agilent with an integration sphere. To assess the outputs of different solar cell devices, illuminated J-V electrical measurements were performed using a WACOM dual lamp solar simulator at standard test conditions (AM1.5G spectrum, 1,000 W/m^2, 25°C). External quantum efficiency (EQE) measurements were carried out with an RR-2100 system from LOT Oriel.

The experimental results of different MQW solar cells devices were analyzed via a combination of optoelectronic modelling approaches. On the one hand, optical modelling was done into a 1D transfer matrix method using the wave-optic-based software package Scout/CODE (by W. Theiss Hardware and Software) by implementing the experimental data of refractive (n) and extinction (k) coefficients for different functional layers.[40] Then, a global matrix was generated for the calculation of the local reflection and transmission coefficients by solving the Fresnel equations at the interfaces between different layers considering the associated matrices to the propagation of the electromagnetic field (light) through each film of the device. As optical modelling outputs, the distribution of the optical field and the local absorption as well as the generated photocurrent can be determined. On the other hand, the electrical simulation was established in AFORSHET (automat for simulation of heterostructures) software after the implementation of the electronic parameters of different functional layers in different MQW device structures.[41] Based on drift-diffusion model, this numerical program solved the semiconductor equations including Poisson's, transport and continuity equations for charge carriers. Then, the energy band diagrams can be computed for the analysis of the electronic collection and transport mechanisms. Detailed inputs of the optoelectronic numerical simulation can be found in Table S3 as well as in previous works.[21,23]

3 | RESULTS AND DISCUSSIONS

3.1 | Synergy between photonic and quantum confinements in ultrathin MQW Si/Ge solar cells featuring photonic nanocavity

In this section, the synergetic impact of both photonic and quantum confinements in ultrathin MQW Si/Ge solar cells are introduced.

3.1.1 | Photonic confinement in ultrathin MQW Si/Ge solar cells

Figure 1a shows the structure of superstrate n-i-p QW solar cell based on a-Si:H (QB)/a-Ge:H (QW) nanostructures. The photoactive material forming the optical absorber is in the order of 20 nm, while the total thickness (h) of the cell core remains below 50 nm which is significantly smaller than the incident optical wavelength (λ). In such device configuration, lossy a-Si:H/a-Ge:H multilayer with high and comparable refractive and extinction indices ($n \sim k \sim 4$) is embedded between transparent front AZO film and Ag metallic back reflector as two regions with lower refractive-indices ($n < 2$). The dispersion relations of refractive index n and extinction coefficient k for different functional layers in ultrathin MQW Si/Ge solar cell devices are plotted in Figure S1. Such architecture with ultrathin and highly lossy films and opaque reflecting metal surfaces, forms an "asymmetric Fabry-Perot (F-P)" deep-subwavelength nanophotonic cavity.[14,15] A detailed theoretical background of the absorption enhancement in optical planar nanocavity can be found in the Section S5 of supporting information as well as in previous papers.[7,15,16,23] The light confinement into small spatial dimensions by resonant recirculation is enabled because of multiple passes of light beam and coherent superposition of the reflected and transmitted electromagnetic fields.[15]

When an incident light beam penetrates the solar cell through the front side, three different phase shifts can occur i.e. the reflection phase shifts at both front ($\phi_{AZO/a\text{-}Si}$) and back ($\phi_{a\text{-}Si/Ag}$) interface edges as well as the round-trip propagation ($\phi_{propagation}$) across the n-i-p functional layers of cell device.[15,42,43] Because of the significant difference in refractive index, the reflection phase shifts are mainly considered at both photonic resonator edges in the vicinity of Ag back and AZO front contacts.[44] Whereas the reflections at the interfaces between the a-Si:H and a-Ge:H absorbing semiconductor multilayer are assumed negligible because of comparable refractive index values.[6] Through the nanophotonic cavity length, the lossy media is characterized by an effective index as an average of optical indices of a-Si:H layers and a-Ge:H QWs weighted by their corresponding thicknesses.[45] In addition, the change of the optical properties of a-Ge:H QWs as a function of thickness because of quantum-size effects must be considered.[23] Considering the ultrathin ($L < < \lambda$) and highly lossy ($n \sim k$) a-Si:H/a-Ge:H multilayer with high absorption coefficients, negligible accumulated propagation phase shift is obtained in the asymmetric subwavelength F-P nanocavity.[14,15] With a highly reflective metallic mirror, a compensation (cancellation) between the

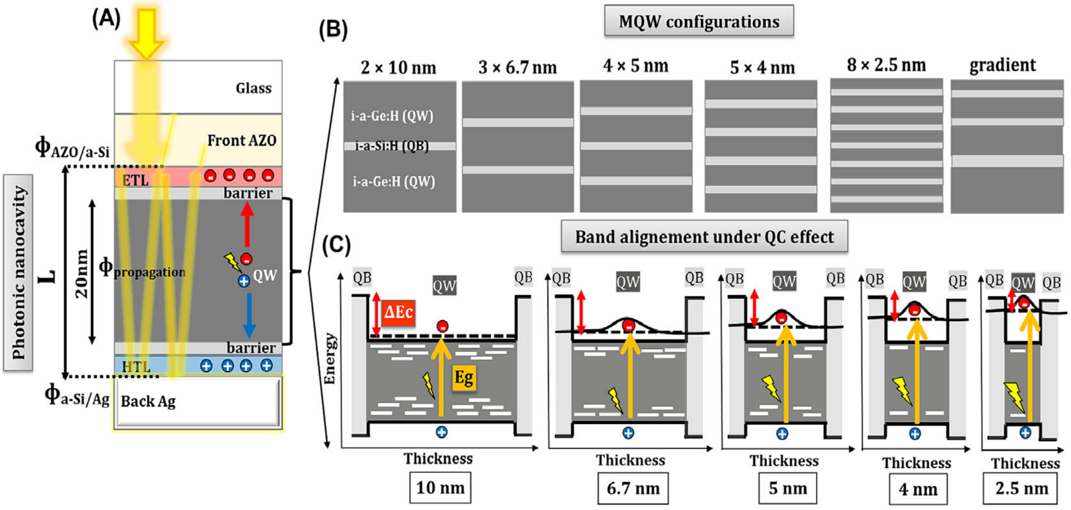

FIGURE 1 Synergy between optical and electronic confinements in ultrathin MQW Si/Ge solar cells. (A) Schematic of n-i-p solar cell device based on a-Si:H (QB)/a-Ge:H (QW) nanostructures embedded as an absorbing optical nanocavity. The multiple passes of light inside the nanophotonic cavity are highlighted by yellow arrows. ($\phi_{AZO/a\text{-}Si}$), ($\phi_{a\text{-}Si/Ag}$) ($\phi_{propagation}$) stand for the reflection phase shift at front and back edges as well as the round-trip propagation across the optical nanocavity, respectively. L is the total thickness of n-i-p multilayer forming the nanocavity length. (B) Illustration of different MQW configurations in real space. (C) Illustration band alignment of a-Si:H (QB)/a-Ge:H (QW) heterostructures in energy space under quantum confinement effects as a function of QW thickness. ΔE_c is the conduction band discontinuity and E_g is the bandgap energy.

reflection and propagation phase shifts takes place, leading to a non-trivial net reflection phase shift (different from 0 and π) at the interface between Ag metal and semiconductor layers.[14,15,46] It follows that the iteration of one-dimensional destructive interferences between incident and reflected light waves generates multiresonant light trapping and multiple passes circulation which maximizes the amount of light absorption in ultrathin photoactive materials because of the field build-up through the nanophotonic cavity.[11,15] Hence, this enables strong absorption resonance (i.e. maximum absorption and minimum reflection) and angle robustness.[15,19,47,48]

The absorption resonance condition corresponds to the situation where the net reflection phase shift including the sum of the two front and back reflection phase shifts ($\phi_{AZO/a\text{-}Si}$) and back ($\phi_{a\text{-}Si/Ag}$) as well as the round-trip propagation phase shift ($\phi_{propagation}$) is a factor of 2π[15]:.

$$\Phi_{AZO/a-Si} + \Phi_{a-Si/Ag} + 2\Phi_{propagartion} = 2m\pi \qquad (1)$$

where m in an integer related to the resonance order. Thus, an optimum combination of nanocavity thickness ($L_{nanocavity} < <\lambda$) and its effective refractive index ($n_{eff,nanocavity}$) is desired to maximize the absorption.[15] This will be further elucidated via optical modelling of different MQW solar cell configurations in terms of optical field and local absorption distributions.

3.1.2 | Quantum confinement in ultrathin MQW Si/Ge solar cells

As depicted in Figure 1B, the single QW nanoabsorber with a total thickness of 20 nm is replaced by different periodic MQW configurations. By keeping a constant 1 nm-thick QB interlayer, the following QW periods are adopted: (2 × 10 nm), (3 × 6.7 nm), (4 × 5 nm), (5 × 4 nm), (8 × 2.5 nm). For different periodic MQW configurations, the energy band alignment consists of periods including narrow-bandgap QW sandwiched between two wide-bandgap QBs, duplicated according to the number of QWs. Furthermore, a gradient-bandgap MQW structure with gradual QW thickness increase (2.5 nm /4 nm /5 nm/6.7 nm) from the front to the back of the device is also considered. Accordingly, the sequence of the bandgaps across the nanobsorber follows a descending order from higher values at the side of the device facing the light source, toward lower values at the adjacent region to the back reflective contact. A detailed theoretical background of quantum-size effects in a-Si:H (QB)/a-Ge:H (QW) nanostructures and the main implications on the quantization of energy levels, the density of states and the electronic transitions can be found in supplementary Section S4 as well as in previous publications.[20,22,24,49] Importantly, the reduction of a-Ge:H QW thickness induces a bandgap widening due an upward shift of the conduction band edge to higher discrete energy level.[49–53] Therefore, QC effects enable significant bandgap engineering in ultrathin MQW Si/Ge solar cell by altering both the QW bandgap E_g and the conduction band offset ΔE_C at the a-Si:H (QB)/a-Ge:H (QW) heterojunction, as shown in Figure 1C.[21] Based on the UV–VIS and ellipsometry optical measurements reported in our previous works, the values of E_g are 0,99 eV, 1,03 eV, 1,09 eV 1,13 eV, 1,18 eV, and 1.3 eV for QW thicknesses of 20 nm, 6.7 nm, 10 nm, 5 nm, 4 nm and 2.5 nm, respectively. Given a QB bandgap of 1.7 eV and a fixed valence band offset $\Delta E_v = 0.15$ eV, this corresponds to ΔE_C values of 0.56 eV, 0.52 eV, 0.46 eV, 0.42 eV, 0.37 eV, 0.25 eV, respectively.[21,23] The thickness-dependent variations of QW bandgap

E_g and conduction band offset ΔE_C at a-Si:H (QB)/a-Ge:H (QW) heterojunction are plotted in Figure S2.

3.2 | Experimental characteristics of different ultrathin MQW Si/Ge solar cells

Herein, the experimental performance outputs of the fabricated devices are presented. Figure 2A showcases the EQE spectra of different ultrathin MQW solar cells. On the one hand, the broadest EQE is obtained for SQW (1 × 20 nm) with the smallest bandgap. While a blue-shift of the absorption onset is manifested as QW thickness reduces because of the bandgap widening under quantum-size effects. This leads to a photocurrent loss at long wavelengths in MQW configuration with the thinnest QW (8 × 2.5 nm) compared to thicker QW counterparts with broader EQE profiles. Moreover, by reducing QW width, a slight deviation to short wavelengths can be noticed for the maximum EQE peak which characterizes the absorption resonance. On the other hand, comparable EQE level of about 60% is reached for all MQW configuration with a slight drop as QW thickness decreases. This is a clear indication for a collective contribution of MQW nanoabsorbers in different configurations to the total photocurrent. In accordance to EQE evolution, a slight increase in the reflection, mostly in the long wavelength range beyond 600 nm is noticed, as the QW period gets narrower. This is a further indication of the absorption drop at the expense of higher reflection by approaching the corresponding absorption onset of each MQW configuration. The aforementioned results are relevant for periodic MQW devices. However, for the gradient-bandgap MQW architecture, the turn-on absorption threshold is similar to MQW (3 × 6.7 nm), implying that the absorption threshold in the case of multiple nanoabsorbers with different bandgaps is imposed by the thickest QW with the narrowest bandgap. For all MQW configurations, the difference between measured EQE and (1-R) spectra confirms the charge extraction deficit in the corresponding solar cell devices.

Figure 2B shows the J-V curves under illumination for different configurations of MQW solar cells. The corresponding performance characteristics are plotted in Figure 2C–F. In accordance with EQE results, the short-circuit current (J_{SC}) values rise progressively from 16.5 mA/cm^2 up to 20.4 mA/cm^2 when QW thickness is increased from 2.5 nm to 20 nm. While, J_{sc} values remain comparable for large QW periods, a remarkable decrease is particularly noticed for the thinnest L_{QW} of 2.5 nm. The J_{sc} values increase in MQW configurations with wider QW periods due to additional absorption of low-energy photons in the lower band-gap QWs. However, an opposite trend is obtained for open-circuit voltage (V_{oc}) and Fill factor (FF) evolution where thinner QWs lead the higher values. Relative improvements of about 60% in V_{oc} and 35% in FF are attained by just changing the MQW period. In combination, the best PCE above 5.5% is achieved with MQW (8 × 2.5 nm), corresponding to a relative enhancement close to 70% compared to the lowest PCE of about 3.3% with MQW (2 × 10 nm). As for gradient-bandgap MQW configuration, V_{oc} value is similar to MQW (3 × 6.7 nm) implying that the photovoltage in case

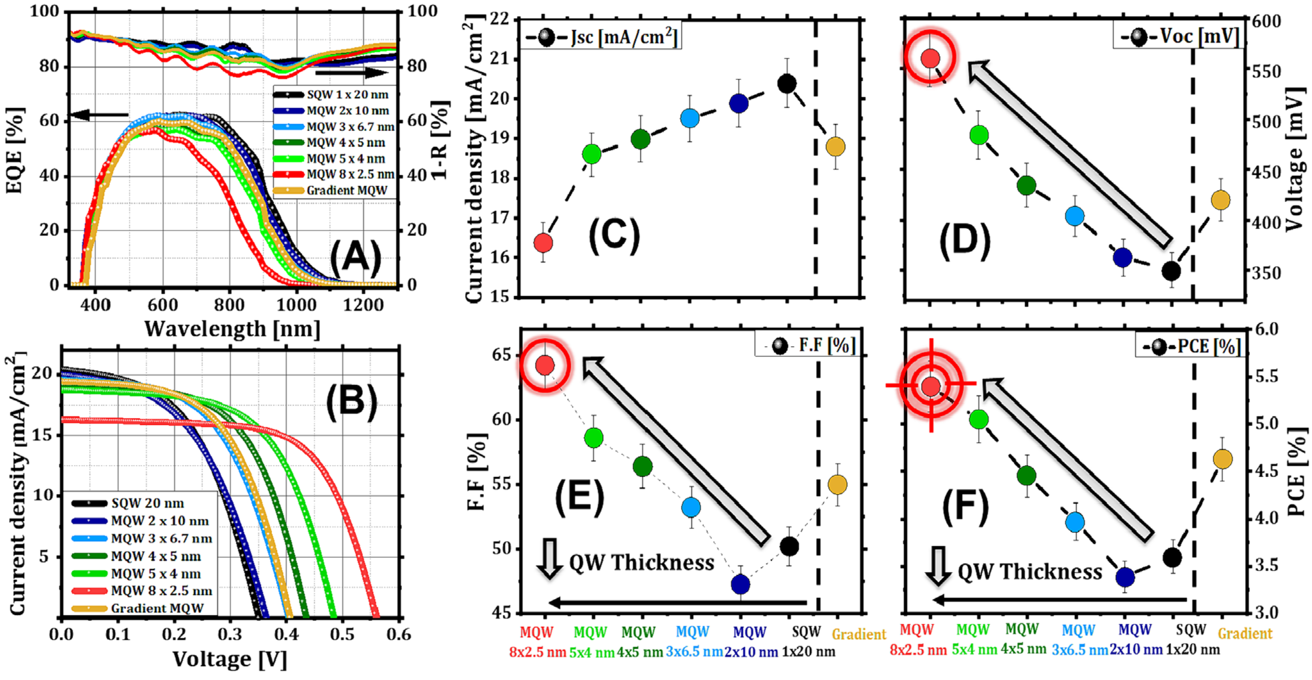

FIGURE 2 Experimental outputs of different configurations of ultrathin MQW Si/Ge solar cells (A) EQE; (B) illuminated J-V curves; the solar cell characteristics as a function of MQW configuration. (C) J_{sc}: short-circuit current, (D) V_{oc}: open-circuit voltage, (E) FF: fill factor and (F) PCE: Photoconversion efficiency. The red circle highlights the best efficiency among different MQW configurations.

of multiple nanoabsorbers with different bandgaps is controlled by the narrowest bandgap of the thickest QW. While FF is slightly better that MQW (3 × 6.7 nm) because of the reduction of carrier transport obstruction at lower potential barrier adjacent to thinner QW.

It is important to disentangle FF and V_{oc} losses by distinguishing between the effects related to carrier escape and energy bandgap tuning. An intriguing observation that confirm this aspect is the comparison of V_{oc} and FF outputs of thick QW devices. Although, MQW (2 × 10 nm) yields higher V_{oc} due to slightly wider bandgap compared with SQW (1 × 20 nm), the corresponding FF value is conversely lower because of the existence of additional intermediate barrier. In contrast, even by multiplying the number of QWs and corresponding QW/barrier heterointerface, the configuration of MQW (8 × 2.5 nm) with thinner QWs and lower potential barrier height still deliver the highest FF. This is a clear indication that FF parameter in Si/Ge MQW solar cells is predominately imposed by large potential barriers causing a blocking of carrier transport and difficulty in collection process.

Further information can be deduced from the rectifying dark J-V characteristics of different MQW solar cell configurations in Figure S4. In the linear plot, it is clear that dark current is sensitively influenced by the bias voltage, especially in MQW configurations with thicker QWs. This points out the crucial role of applied electric field in the extraction and sweeping of the charge carriers out of amorphous QWs and in the drift-assisted carrier collection across intrinsic MQW depletion region of n-i-p diode.[54] In log scale plot, it can be noticed that the dark currents drop gradually over the entire voltage range when QW periods get thinner, confirming lower resistive losses and better carrier transport.[55,56] In particular, the reduction of dark current implies lower non-radiative recombination rate across the intrinsic MQW region via defects through gap states of semiconductor layers and at the heterointerfaces.[57,58] This proves that lowering the potential barrier height at QW/QB heterojunction in MQW region controls the mitigation of recombination processes, leading to facilitated carrier escape and reduced of resistive losses.[59] It is worth mentioning that thinner nanoabsorbers relative to the diffusion/recombination length of the charge carriers promote short escape times and elevated velocities under applied electric field.[60]

The significant aforementioned variations in the experimental results of different ultrathin MQW Si/Ge solar cells point out the importance of the understanding of optical design and bandgap engineering in our emerging PV technology. Therefore, in the following sections, the output characteristics of solar cell devices will be explained based on optoelectronic modelling.

3.3 | Bandgap engineering in ultrathin MQW Si/Ge solar cells

Considering the described physical mechanisms in Figure S5 from the supplementary Section S7, we analyze the photogeneration, recombination and transport mechanisms via optoelectronic modelling and experimental measurements to further elucidate the devices operation.

3.3.1 | Open-circuit voltage in ultrathin MQW Si/Ge solar cells

In order to explain the photovoltage change for different n-i-p MQW configurations, band diagrams at the corresponding V_{oc} conditions are computed with numerical simulation (Figure 3), considering the band alignments depicted in Figure 1C. The calibration and validation of optoelectronic modelling with J-V experimental results for different Si/Ge MQW device configurations is presented in Figure S6. As explained in supplementary information S6 related to physical mechanisms in ultrathin Si/Ge MQW solar cell, the supplied V_{oc} voltage is linked to the absorber bandgap E_g and depends on the effective density of states, and the effective generation and recombination rates of free charge carriers, as follows[61]:.

$$qV_{oc} = E_g + K_B T \frac{N_c N_v}{n_g p_r} \tag{2}$$

where q is the elementary charge, N_c and N_v denote the effective density of states of the conduction and valence bands, respectively, n_g and p_r are related to the effective generation and recombination rates of free charge carriers, respectively. Indeed, the photovoltage of MQW solar cell device is directly linked difference of quasi-Fermi levels between electrons ($E_{F,n}$) and holes ($E_{F,p}$) determining the electrochemical potential of electrons/holes and the occupation of states between the conduction and valence bands.[62] Hence, the most important finding is that, in periodic MQW structures, thinner QWs with larger bandgap yield higher V_{oc} values. This is induced by the large spatial splitting of the quasi-Fermi levels between $E_{F,n}$ (electrons) and levelled down $E_{F,p}$ (holes) because of bandgap widening under QC effects, as can be clearly observed when QW thickness decreases from 10 nm down to 2.5 nm. This implies a promoted separation of the photogenerated carriers because of better asymmetric conductivities, as well as minimization of recombination between opposite electrons and holes leading to longer electron lifetime in MQW configurations with thinner QWs.[50,63] Wider QWs with deeper conduction band prolong the escape time of electrons, leading to higher recombination and lower V_{oc}.[64] Interestingly, the V_{oc} improvement in thinner QW was previously demonstrated in single QW solar cell devices and it is further confirmed to be also valid in MQW solar cell devices.[21] In gradient MQW configuration, the splitting of quasi-Fermi level and hence V_{oc} value is governed by the thickest QW with narrower E_g adjacent to the back side of solar cell device. The aforementioned interpretations based on numerical simulation for the dependence of V_{oc} on the QW thickness in MQW devices, are consistent with experimental J-V results shown in Figure 2B and D. It is noteworthy that coupling of QWs when employing ultrathin QBs can alter the bandgap because of the formation of mini-bands by wavefunction overlapping in superlattice-like band structure.[52] This points out the importance of studying the impact of QB thickness variation in further works related to Si/Ge MQW solar cells. Based on the experimental dark and illuminated J-V results, even though MQW configuration (8 × 2.5 nm) with thinner period yields the highest

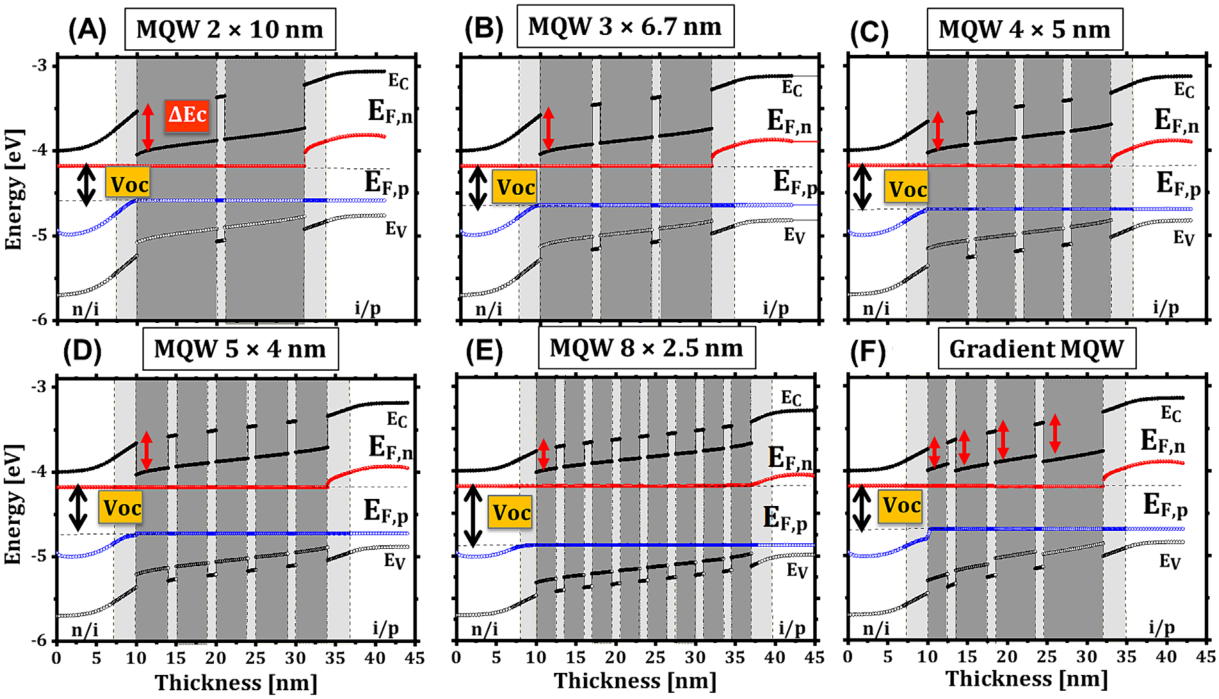

FIGURE 3 Energy band diagram at open circuit conditions for different n-i-p MQW configurations. (A) MQW 2 × 10 nm, (B) MQW 3 × 6.7 nm, (C) MQW 4 × 5 nm, (D) MQW 5 × 4 nm, (E) MQW 8 × 2.5 nm, (F) gradient MQW. The band gap energy of QW E_g and the QW/barrier conduction band offsets ΔE_c are highlighted with black and red arrows, respectively.

photovoltage owing to bandgap widening, it is noticed that V_{oc} parameter is still a limiting factor because of the multiplication of the recombination sites at the QW/barrier heterointerfaces. In this regard, it is expected that the enhancement of passivation at QW/QB heterointerfaces by post-treatments during the fabrication process could minimizes the recombination defects and hence, improve the overall V_{oc}.[65] Thus, we estimate that the achieved efficiency can be further improved by boosting V_{oc} output, while preserving similarly high J_{sc} and FF achieved for ultrathin Si/Ge MQW solar with the thinnest QW.

3.3.2 | Fill factor in ultrathin MQW Si/Ge solar cells

As explained in supporting information S6 on the physical mechanisms in ultrathin Si/Ge MQW solar cell, the change of the conduction band discontinuity at the a-Si:H (QB)/a-Ge:H (QW) heterojunctions under QC effect strongly affects the sequential carrier transport and collection behavior. Mainly, the FF parameter is strongly dependent on the V_{oc} and is dominated by the carrier transport and the resistive losses at the junctions. Therefore, it is evident that lower V_{oc} values for MQW configuration with wider QWs directly leads to reduced FF. Moreover, a reduction of the potential barrier height between a-Ge:H QW and a-Si:H barrier is expected to improve the carrier collection by tunneling and thermal emission mechanisms, minimize the resistive losses and hence improve the FF output.

EQE under voltage bias and carrier collection efficiency

To examine the collection processes in solar cell devices with different MQW configurations, the EQE spectra at varied voltage bias are displayed in Figure 4A–F. Broader and more intense EQE profiles are obtained for MQW configurations with thicker QW periods. Slight enhancements in quantum efficiency of different MQW devices occur by applying increasingly negative electrical biases. This suggests an increase in the density of photogenerated carriers reaching both front and back transport layers. It is clearly observed that EQE spectra undergo a degradation for positive bias voltages, with more pronounced variation for MQW configurations with thicker QW periods. This can be considered as a signature for the existence of transport barriers at the a-Si:H (QB)/a-Ge:H (QW) heterointerfaces upon the dominant drift-assisted carrier collection in these n-i-p device architectures.[66,67] The configuration with gradient MQW follows similar trend to MQW (3 × 6.7 nm), suggesting that the carrier collection mechanism is dominantly imposed by thicker QWs with narrower bandgap and larger band discontinuity at QW/QB heterojunction. In fact, applying a forward bias weakens the electric field within the intrinsic MQW regions, and declines the carriers escape from QWs in the drift transport.[68,69] Also, the recombination rate increases when more carriers flow into the intrinsic MQW region with higher forward bias.[64] The hindrance of carriers sweeping out of QWs leads to eventual recombination events, and hence, a drop in the generated current at forward bias.[68,69] Therefore, the degradation of EQE under forward bias, especially for thick QW periods, is an indication of deficient carrier collection at low electric field.[67–69]

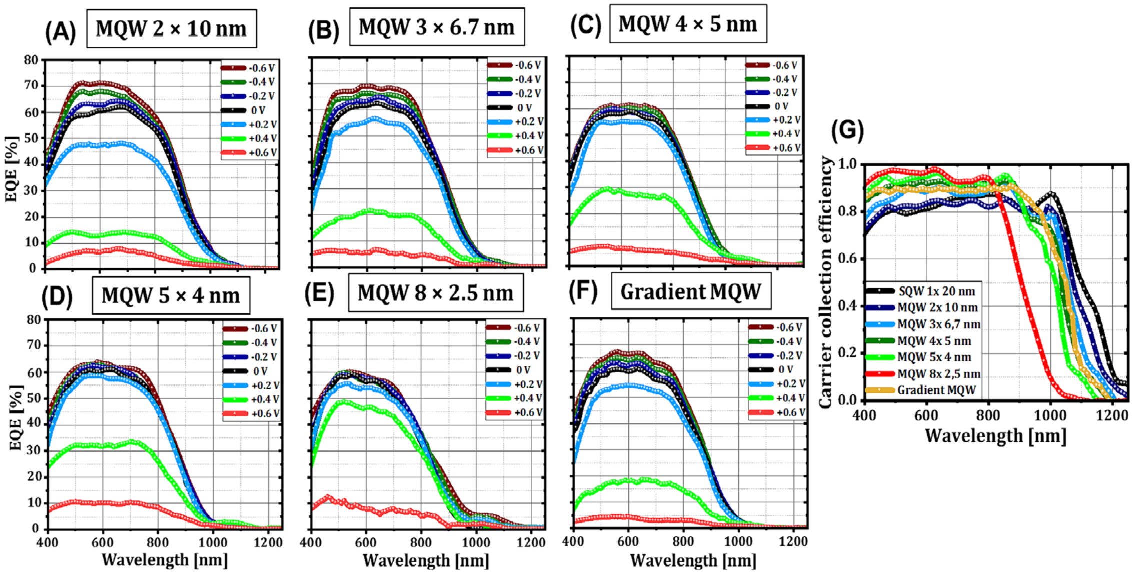

FIGURE 4 EQE extracted from spectral response measurements at varied voltage bias on devices with different MQW configurations. (A) MQW 2 × 10 nm, (B) MQW 3 × 6.7 nm, (C) MQW 4 × 5 nm, (D) MQW 5 × 4 nm, (E) MQW 8 × 2.5 nm, (F) gradient MQW. (G) Carrier collection efficiency (CCE) for all MQW configurations with reverse bias of - 0.6 V.

To effectively assess the efficiency of carrier transport in quantum nanostructured solar cells, the parameter of carrier collection efficiency (CCE) can be defined, referring to the fraction of photogenerated carriers that are collected as photocurrent.[68] Since large fraction of photogenerated carriers can be collected from the MQW under sufficient reverse bias because of high electric field, the CCE can be determined via a normalization of the illumination-induced current enhancement to the corresponding saturation value at reverse bias, as follows[33,68]:.

$$CCE\,(V,\lambda) = \frac{EQE\,(V,\lambda)}{EQE\,(V_{reverse},\lambda)} \tag{3}$$

where EQE (V, λ) is the external quantum efficiency at a given illumination wavelength and bias voltage, EQE ($V_{reverse}$, λ) is the EQE obtained at sufficiently high reverse bias of −0.6 V in this case. In Figure 4G, the spectral variation of CCE for solar cells with different MQW configurations is depicted. The shift of the absorption threshold to shorter wavelengths by decreasing QW thickness affect in turn the edge of CCE spectra. Importantly, it is clearly noticed that CCE improves at the corresponding spectral absorption range of different MQW configurations when the thickness of QW period decreases. This means that the fraction of photogenerated carriers contributing to photocurrent under strong electric field is higher for MQW with the thinnest QW periods because of better carrier transport compared to thicker counterparts.

A simplified picture of possible microscopic collective charge carrier dynamics and electronic transport mechanisms in a-Si:H/a-Ge:H MQW solar cell using semi-classical drift -diffusion modelling is provided in supporting information S6. This includes the spatial distributions of electrons and holes densities, the current densities, the recombination rates and the electric field distributions for different MQW configurations at their corresponding maximum power point (MPP) conditions under AM1.5G spectrum. Further insights into the transport mechanisms in our ultrathin Si/Ge MQW solar cell beyond semi-classical drift-diffusion model can be gained in case of using advanced microscopic quantum kinetic approaches in prospective works.[70–75]

General interpretations from microscopic collective charge carrier dynamics and electronic transport mechanisms in ultrathin Si/Ge MQW solar cell

Given the small forward voltage bias at each MPP condition, the diffusion of majority carriers into the intrinsic MQW region gives rise to forward dark current in opposite direction to the solar cell current flow. While, a diffusion of minority carriers occur from the opposite doping polarity toward the space charge region.[64]

In Figure S7, steeper decrease in electron current density across the intrinsic MQW region for thicker QW periods (MQW 2 × 10 nm) compared to thinner QW counterparts, reaching a minimum level around the middle nanoabsorber positions. This is a possible indication of the deficiency of electrons collection in wide QWs because of the blocking by large potential barrier which inhibits the escape process and the increment of photocurrent flowing through the QWs. Such interpretation is consistent with the lowest FF value in Figure 2E obtained for the solar cell device with MQW (2 × 10 nm).

In the MQW regions, the escape conduction mechanisms of photogenerated carriers can occur either by the tunneling or thermionic emission processes, as explained in Section S6.[76,77] For the thermal transport mechanism, it is strongly dependent on the potential height as the charge carriers are compelled to overcome over the top of barrier by means of thermal kinetic energy. This implies that the change of barrier height and applied electric field affects the occurrence of thermal escape mechanism. As for tunneling transport mechanisms, the transmission probability and the escape time is dependent on the barrier height and thickness.

Therefore, the reduction of potential barrier height at the conduction band of a-Ge:H (QW)/a-Ge:H (QB) heterojunction under QC effects, leads to improved carrier collection by both tunneling and thermal emission processes (Figure S5). This is consistent with the experimental FF results in Figure 2E.

Within the intrinsic MQW region, both dominant recombination forms including band-to-band radiative (R_{rad}) and trap-assisted Shockley-Read-Hall (R_{SRH}) non-radiative are strongly correlated to the electrons n and holes p carrier populations, as described in Section S7.[67]

It was reported that the spatial profiles of carrier densities and the distribution of the majority/minority carriers govern the collection and the recombination processes in the intrinsic MQW region. In fact, photogenerated electrons tend to recombine in the region with opposite polarity i.e. hole-rich region, whereas, photogenerated holes are more susceptible for recombination in electron-rich region. Hence, the average transport distance and the drift length of the minority carriers are the shortest in the regions with symmetric carrier distribution ($n = p$), which detrimentally affects the collection process. The collection of photogenerated carriers near to the front (back) side of the MQW region is limited by the hole (electron) transport in the n-rich (p-rich) zone toward the hole-selective (electro-selective) contacts.[33] In contrast, the majority carriers in each section can be better extracted out of the QWs. An increment of R_{SRH} recombination rate is expected because of a variation in the electron density Δn in hole-rich region ($p > n$).

The recombination rate is known to increase with higher carriers flowing within the intrinsic MQW region under voltage bias at MPP condition.[64] By increasing the thickness of QW, the extension of the recombination volume causes further deficiency of the electronic transport because of the detrimental effects on the travel, the scattering dynamics and the lifetime of the charge carriers.[64,78] Considering the competition between the photocarrier escape and recombination within QW regions, thick QWs with high potential barriers at the conduction band result in longer trapping/capture time of electrons, preventing their escape from the QW to contribute in the photocurrent.[64,79] Whereas, thinner QWs with small potential barriers lead to promoted separation of the photogenerated carrier with minimal recombination, longer carrier lifetime and better lateral conductivity.[50,63]

For MQW nanostructures in n-i-p architecture with dominant drift-assisted carrier collection, the internal electric field is crucial for the extraction and the sweeping of the charge carriers out of the amorphous QWs materials with limited diffusion length.[64,67,79] A sufficient electric field is required to prevent the capture and recombination of the escaped carriers from QWs.[64,79] In contrast, the internal electric field can be deformed under the effect of trapping recombination sites within MQW region.

The escape mechanism in low field is dominated by the density of electron states near the top of QW. For thinner QWs, the transport of electrons is ensured by drift transport under sufficient electric field in the intrinsic MQW region.[64] Shorter escape times for electron is assumed in narrower QWs with uplifted conduction band and higher electric field.

To this end, the disparity in electronic collection and transport mechanisms between MQW configurations with different periods induces FF changes (Figure 2E) in the corresponding ultrathin Si/Ge MQW solar cells.

3.4 | Optical design in ultrathin MQW Si/Ge solar cells

It is well-known that the photocurrent of a solar cell device is directly linked to the optical absorption spectrum of the photoactive absorber. The total current densities at short-circuit condition J_{sc} is related to the solar spectrum AM 1.5G and the EQE of solar cell devices (Figure 2A), given by integrating J_{sc} (λ) at each specific wavelength over the absorption spectral range:

$$J_{sc} = \int \frac{e\lambda}{hc} EQE\,(\lambda) I_{AM1.5}(\lambda) d\lambda \tag{4}$$

where $I_{AM1.5}(\lambda)$ is AM 1.5G solar radiation spectrum and e, h, λ and c are elementary charge, Plank constant, wavelength, and speed of light, respectively. It follows that the supplied current density is linked to the absorptance determined by the nanoabsorber thickness and its absorption coefficient. In the following parts, we investigate the impact of optical design of nanoabsorbers in terms of MQW configurations and QW numbers on the distribution of the optical field and the local absorption. This allows to explain the change in photocurrent generation of different ultrathin MQW Si/Ge solar cells by optical modelling in the light of the experimental EQE results presented in Figure 2A.

Across the MQW solar cell device, the optical absorption in different functional layers mainly depends on the amplitude of light electromagnetic field and on the optical refractive indices (n, k) of materials, given by[16]:

$$Absorption\,(z,\lambda) = \frac{2\pi c\,\varepsilon}{\lambda} n(z,\lambda) \times k(z,\lambda)\,|E(z,\lambda)|^2 \tag{5}$$

where c is the speed of light, ε is the permittivity of free space and $|E(z,\lambda)|^2$ is the electric field amplitude as a function of depth z and wavelength λ.

Based on the electric field map of spatial and spectral distribution displayed in Figure S8 from supporting information, the evolution of the maximum amplitude of the normalized optical field at individual light wavelengths across the depth of each ultrathin Si/Ge MQW solar cell configuration is extracted in Figure 5. The range of wavelengths covers visible and NIR from 400 nm to 1,000 nm with an increment of 100 nm. The zero-position is considered at the Ag/p-a-Si:H interface in the back edge of nanophotonic cavity. At this metallic back contact,

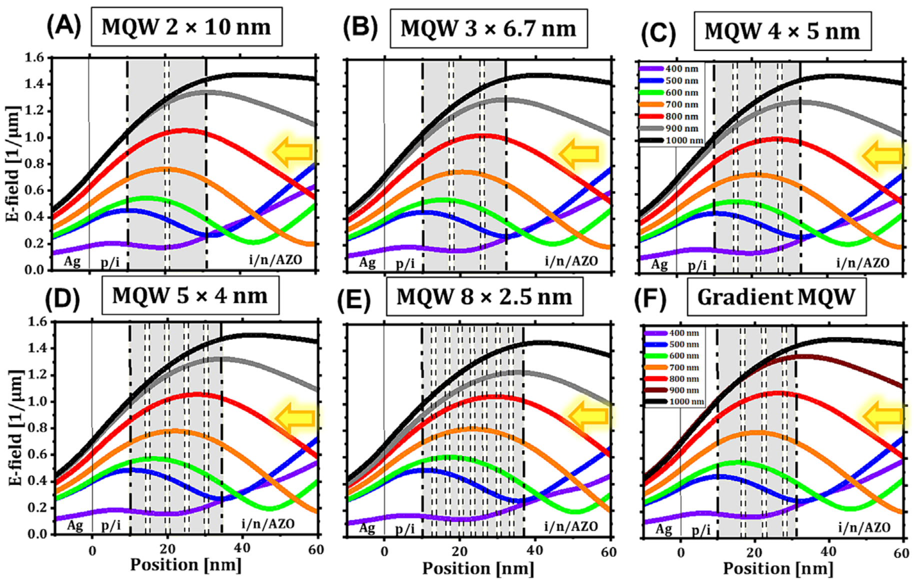

FIGURE 5 Spatial distribution of electric field for individual optical wavelengths across the depth of each configuration of ultrathin Si/Ge MQW solar cells separately. (A) MQW 2 × 10 nm, (B) MQW 3 × 6.7 nm, (C) MQW 4 × 5 nm, (D) MQW 5 × 4 nm, (E) MQW 8 × 2.5 nm, (F) gradient MQW. Dashed lines and grey zones indicate the MQW region in each device configuration. Yellow arrows show the direction of the incident light.

the electric field is attenuated for all solar cells once penetrating Ag medium because of skin effect, with more pronounced decay for shorter wavelengths.[16] Then, a rise in the electric fields of all wavelengths take place through the p/i a-Si:H layers, with more significant change for longer wavelengths. Within different MQW regions outlined with dashed lines and grey boxes, the intensity of electric field increases gradually from shorter to longer wavelengths. By placing the MQW intrinsic zones in centered positions relative to the edges of the photonic absorbing nanocavity, the intensity maxima of the electric field for all wavelengths occur within the nanoabsorber regions.[80] However, the positions corresponding to maximum peak intensities displace from the back sides to front sides of different MQW devices as the light wavelengths increase from shorter to longer values. The maximum intensities of the electric field for short wavelengths ($\lambda < 600$ nm) are low and remain near to the Ag back side. Whereas, the zones with high electric field intensity are more spatially spread within MQW regions in the case of longer wavelengths.

To visualize the spatial propagation of light waves, the optical field variations for separate specific wavelengths across the depth of all MQW solar cell devices are simultaneously compiled in Figure S9. It is clearly noticed that the amplitude of electric field at each wavelength is very similar among all MQW solar cell devices. This is in accordance with comparable EQE levels (Figure 2A) for different MQW configuration within their absorption range. However, the slight thickness extension in the case of MQW periods with larger QW numbers is accompanied with a decrease in the electric field intensity for all wavelengths in the vicinity of the i/n regions. This is expected to induce lower absorption efficiency in the top parts of QWs near to the front side of solar cell devices, especially for MQW (8 × 2.5 nm). These observations are consistent with the comparable EQE at short wavelengths and the incremental disparity between MQW configurations for longer wavelengths above 600 nm.

Next, we examine the distribution of local absorption as a function of wavelengths and across the depth of ultrathin Si/Ge MQW solar cells with different configurations in Figure 6. The regions with high absorption require a simultaneous combination of strong electric field intensity$|E(\lambda)|^2$ and lossy materials with higher product of refractive indices $n(\lambda) \times k(\lambda)$. In the spatial wavelength-dependent distributions, suitable spectral and spatial overlapping of electric field maxima with medium having high refractive indices in the photoactive MQW regions is desired to foster photocurrent generation.

In all MQW configurations, more intense and broader absorption in obtained for each a-Ge:H QW region because of higher product of optical coefficients $n(\lambda) \times k(\lambda)$ and lower bandgap energy E_g compared to other a-Si:H buffer or barrier functional layers (Figure S1). This implies dominant contributions of a-Ge:H QW regions with all different thicknesses in the generated photocurrent from the intrinsic photoactive absorbers of different MQW solar cells.

Another observation is that the high-absorption regions (red zones) are spectrally spread to long wavelengths beyond 700 nm for MQW configurations with QW thicker than 5 nm, but, these sections with intense absorption get restricted to wavelengths around 600 nm when QW thickness is reduced down to 2.5 nm. A fascinating aspect in variation the local absorption with different MQW configurations is manifested for the spatial distribution across the length of photonic nanocavity. This is strongly affected by the electric field distributions, considering the intensity maxima of the electric field for all wavelengths within the nanoabsorber regions and the shift of maximum peak intensities from the back sides to front sides by increasing optical wavelengths. It follows that, along the depth of solar cell devices, the regions of QWs nanoabsorbers in the vicinity of the Ag back reflectors are characterized by the strongest local absorption in all the QW configurations. These high-absorption regions (red zones) are extended up to 30 nm away from the Ag/p-a-Si:H back edge of the nanophotonic cavity. The enhanced optical absorption is a consequential outcome of the strong resonance in the planar nanocavity because of the electric field build-up and interference effects. Then, a gradual decrease in the absorption intensity of all wavelengths is visualized

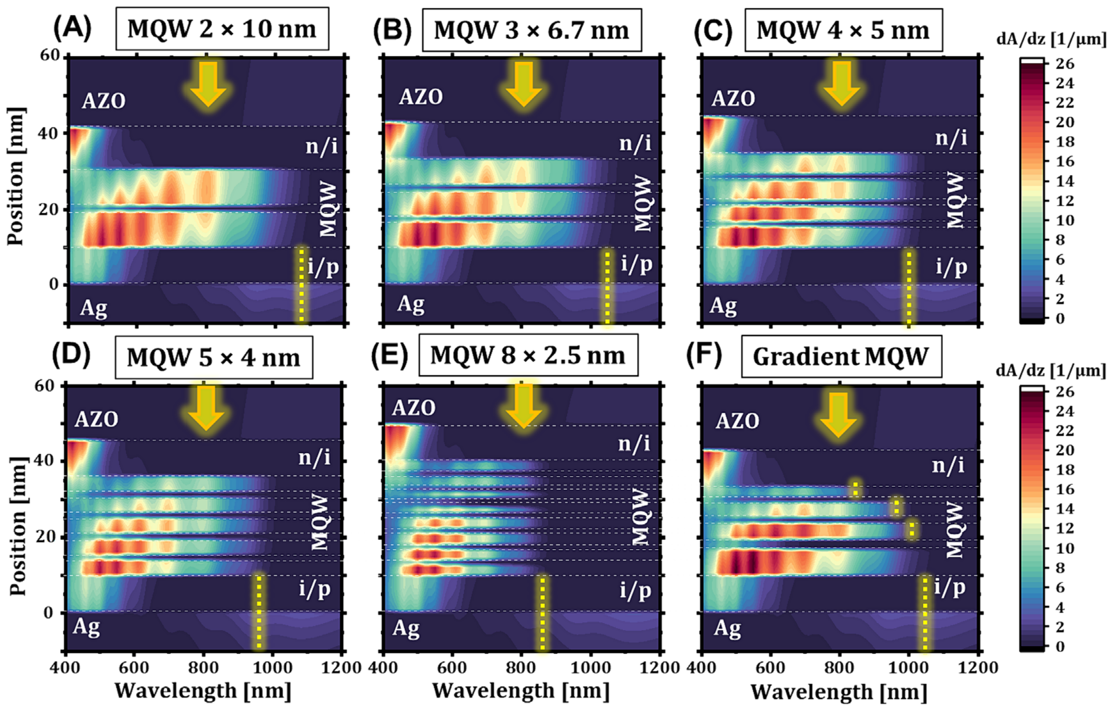

FIGURE 6 Spectral and spatial distribution maps of local absorption as a function of wavelengths and across the depth of ultrathin Si/Ge MQW solar cells with different configurations. (A) MQW 2 × 10 nm, (B) MQW 3 × 6.7 nm, (C) MQW 4 × 5 nm, (D) MQW 5 × 4 nm, (E) MQW 8 × 2.5 nm, (F) gradient MQW. The dashed white lines point out the interfaces between different functional layers. The corresponding absorption thresholds for each a-Ge:H QW thickness is highlighted with dashed yellow lines. Yellow arrows show the direction of the incident light.

over different stratified MQW configurations, when QWs position get further away from the back reflective contact. This is rigorously related to the drop of the electric field intensity near to the i/n layers at front side of the devices for all light wavelengths. The spatial extension of the nanophotonic cavity length maximizes the propagation phase shift, hinders the compensation of nontrivial total phase shift and weakens the light confinement capability by multiple passes recirculation. Therefore, lower absorption is noticed in the QW regions adjacent to the front side, especially, for the MQW configuration (8 × 2.5 nm) with thinner QW thickness/period and large number of QWs. This would induce different partial contributions in the total photocurrent across multiple nanoabsorber regions and a nonproportional dependence of photocurrent as a function of QW number. For gradient configuration (Figure 6f), thicker QW near Ag region is desired to maximize the absorption enhancement inside the photonic nanocavity. In contrast to the adopted gradient configuration, a reversed order with instead thicker QW closer to the AZO front side would suffer from a deficiency in the corresponding local spatial absorption, especially for shorter wavelengths, as can be noticed in Figure S10.

To this end, by changing the period QWs in different MQW configurations with the same total thickness of i-a-Ge:H absorbing material in the range of 20 nm, the values of photocurrent slightly change for large QW period, but, a drop is observed especially for the thinnest L_{QW} of 2.5 nm. The similarity in photogenerated current level can be attributed to comparable round-trip propagation phase shifts controlled by the nanocavity length and the effective refractive index of the absorbing media an average of optical indices of a-Si:H (QB) and a-Ge:H (QW) multilayer weighted by their corresponding thicknesses. This in turn leads to comparable spatial distribution of the corresponding optical field and local absorption. Small difference is caused by the drop of both the electric field and the local absorption near to the i/n layers at front side as MQW thickness gets away from the back reflective edge of the nanocavity. However, the main discrepancy consists of the spectral absorption where the high-absorption regions and the absorption threshold are restricted to shorter wavelengths by decreasing QWs thickness due QC effects. This is the main reason of the photocurrent variation in different MQW configurations. It is noteworthy that the photocurrent is also dependent on the solar spectrum with higher intensities at shorter wavelengths between 450 nm and 650 nm (which is in accordance with EQE curves in Figure 2A). Thus, maximizing the optical absorption at this short-wavelength range it is beneficial to boost the photocurrent.

In a broader context, the optical design considerations deduced along this work remain valid for the development of derived semitransparent devices. For this purpose, further theoretical and experimental analysis about the influence of QW number, barrier thickness and back reflector thickness will be insightful for the optimization of ultrathin semi-transparent Si/Ge MQW solar cells with optimum trade-off between power conversion efficiency and visible light transmission. The presented results also indicate possible further improvements by better matching the zones of high optical field intensity with the QW positions within the nanoabsorber. This could be achieved by the optical design of the functional layers at the front side of the device and, particularly, tuning the thickness of AZO front layer and employing selective contacts with lower parasitic absorption.[81–85]

4 | CONCLUSIONS

In this work, we report the prime study about the implications of different MQW nanoabsorber configurations through optical design and bandgap engineering on the characteristics of ultrathin Si/Ge MQW solar cell devices. By changing the MQW configuration in the deep-subwavelength photonic nanocavity, the interplay of optical and electronic confinements results in large tuning capabilities of the optoelectronic properties.

For the optical aspect, the variation of QW thicknesses and the optical bandgaps in different MQW configurations induces a modulation of the absorption threshold, the resonance condition and the photocurrent output. Based on optical modeling, a detailed analysis of the spatial and spectral distributions of the electric field and the local absorption in different ultrathin Si/Ge MQW solar cells is conducted to further elucidate the optical design considerations.

For the electrical aspect, because of quantum-size effect, the change of individual QW thicknesses in different MQW configurations alters both the bandgap energy of a-Ge:H QW and the band offset at the a-Ge:H (QW)/a-Si:H (QB) heterojunctions. This in turn controls the photovoltage as well as the carrier collection efficiency in solar cell devices.

Owing to the optimization of MQW configuration by adopting thinner QW period inside the absorbing nanocavity with highly reflective Ag mirror, a new record efficiency of about 5.5%, is achieved for this emerging ultrathin Si/Ge MQW PV technology, because of the optimum trade-off between all the characteristic outputs of the corresponding solar cell device.

The design rules of ultrathin amorphous Si/Ge MQW opaque solar cells established in this study are beneficial for the engineering of derived color-neutral, switchable or semi-transparent PV devices integrated in relevant applications like in buildings, vehicles and greenhouses.

ACKNOWLEDGMENTS

The authors acknowledge funding from the Energy branch of the German Aerospace Center (DLR). We would also like to thank M. Götz-Köhler, U. Banik, O. Sergeev, C. Koch, N. Osterthun, L. Busch, N. Neugebohrn, D. Berends and all the group colleagues at DLR Institute of Networked Energy Systems for the insightful inputs. Open Access funding enabled and organized by Projekt DEAL.

DATA AVAILABILITY STATEMENT

The data that support the findings of this study are available on request from the corresponding author. The data are not publicly available due to privacy or ethical restrictions.

ORCID

Hosni Meddeb https://orcid.org/0000-0001-8939-7910

REFERENCES

1. Massiot I, Cattoni A, Collin S. Progress and prospects for ultrathin solar cells. *Nat Energy*. 2020;5(12):959-972. doi:10.1038/s41560-020-00714-4
2. Götz M, Osterthun N, Gehrke K, Vehse M, Agert C. Ultrathin Nanoabsorbers in photovoltaics: prospects and innovative applications. *Coatings*. 2020;10(3):218. doi:10.3390/coatings10030218
3. Traverse CJ, Pandey R, Barr MC, Lunt RR. Emergence of highly transparent photovoltaics for distributed applications. *Nat Energy*. 2017;2(11):849-860. doi:10.1038/s41560-017-0016-9
4. Lee K, Um H-D, Choi D, et al. The development of transparent photovoltaics. *Cell Reports Phys Sci*. 2020;1(8):100143. doi:10.1016/j.xcrp.2020.100143
5. Meddeb H, Götz-Köhler M, Neugebohrn N, et al. Tunable photovoltaics: adapting solar cell technologies to versatile applications (Adv. Energy mater. 28/2022). *Adv Energy Mater*. 2022;12(28):2270121. doi:10.1002/aenm.202270121
6. Steenhoff V, Theuring M, Vehse M, von Maydell K, Agert C. Ultrathin resonant-cavity-enhanced solar cells with amorphous germanium absorbers. *Adv Opt Mater*. 2015;3(2):182-186. doi:10.1002/adom.201400386
7. Wang Y, Shen P, Liu J, et al. Recent advances of organic solar cells with optical microcavities. *Sol RRL*. 2019;3(8):1900181. doi:10.1002/solr.201900181
8. Paliwal A, Dreessen C, Zanoni KPS, et al. Vacuum-deposited microcavity perovskite photovoltaic devices. *ACS Photonics*. 2021;8(7):2067-2073. doi:10.1021/acsphotonics.1c00389
9. Vandamme N, Chen H-L, Gaucher A, et al. Ultrathin GaAs solar cells with a silver Back Mirror. *IEEE J Photovolt*. 2015;5(2):565-570. doi:10.1109/JPHOTOV.2014.2371236
10. Zheng ZW, Yu J, Lai MH, Ying LY, Zhang BP. Efficiency enhancement for resonant-cavity-enhanced InGaN/GaN multiple quantum well solar cells. *Vacuum*. 2017;140:76-81. doi:10.1016/j.vacuum.2016.12.011
11. Ghobadi A, Hajian H, Butun B, Ozbay E. Strong interference in planar, multilayer perfect absorbers: achieving high-operational performances in visible and near-infrared regimes. *IEEE Nanotechnology Mag*. 2019;13(4):34-48. doi:10.1109/MNANO.2019.2916113
12. Chen H-L, Cattoni A, de Lépinau R, et al. A 19.9%-efficient ultrathin solar cell based on a 205-nm-thick GaAs absorber and a silver nanostructured back mirror. *Nat Energy*. 2019;4(9):761-767. doi:10.1038/s41560-019-0434-y
13. Goldman DA, Murray J, Munday JN. Nanophotonic resonators for InP solar cells. *Opt Express*. 2016;24(10):A925-A934. doi:10.1364/OE.24.00A925
14. Kats MA, Blanchard R, Genevet P, Capasso F. Nanometre optical coatings based on strong interference effects in highly absorbing media. *Nat Mater*. 2013;12(1):20-24. doi:10.1038/nmat3443
15. Kats MA, Capasso F. Optical absorbers based on strong interference in ultra-thin films. *Laser Photonic Rev*. 2016;10(5):735-749. doi:10.1002/lpor.201600098
16. Lee K-T, Seo S, Lee JY, Guo LJ. Strong resonance effect in a lossy medium-based optical cavity for angle robust spectrum filters. *Adv Mater (Deerfield Beach, Fla)*. 2014;26(36):6324-6328. doi:10.1002/adma.201402117
17. Park J, Kang J-H, Vasudev AP, et al. Omnidirectional near-Unity absorption in an ultrathin planar semiconductor layer on a metal substrate. *ACS Photonics*. 2014;1(9):812-821. doi:10.1021/ph500093d
18. Song H, Guo L, Liu Z, et al. Nanocavity enhancement for ultra-thin film optical absorber. *Adv Mater (Deerfield Beach, Fla)*. 2014;26(17):2737-2743. doi:10.1002/adma.201305793

19. Zhao J, Qiu M, Yu X, et al. Defining deep-subwavelength-resolution, wide-color-gamut, and large-viewing-angle flexible subtractive colors with an ultrathin asymmetric Fabry–Perot Lossy cavity. *Adv Optical Mater*. 2019;7(23):1900646. doi:10.1002/adom.201900646
20. Barbagiovanni EG, Lockwood DJ, Simpson PJ, Goncharova LV. Quantum confinement in Si and Ge nanostructures: theory and experiment. *Appl Phys Rev*. 2014;1(1):11302. doi:10.1063/1.4835095
21. Meddeb H, Osterthun N, Götz M, et al. Quantum confinement-tunable solar cell based on ultrathin amorphous germanium. *Nano Energy*. 2020;76:105048. doi:10.1016/j.nanoen.2020.105048
22. Yoffe D. Low-dimensional systems: quantum size effects and electronic properties of semiconductor. *Adv Phys*. 1993;42(2):173-262. doi:10.1080/00018739300101484
23. Meddeb H, Gotz-Kohler M, Osterthun N, et al. Investigation of quantum size effects on the optical absorption in ultrathin single quantum well solar cell embedded as a Nanophotonic resonator. *IEEE J Photovolt*. 2022;12(3):760-770. doi:10.1109/JPHOTOV.2022.3150726
24. Edvinsson T. Optical quantum confinement and photocatalytic properties in two-, one- and zero-dimensional nanostructures. *R Soc Open Sci*. 2018;5(9):180387. doi:10.1098/rsos.180387
25. Nozik AJ. Nanoscience and nanostructures for photovoltaics and solar fuels. *Nano Lett*. 2010;10(8):2735-2741. doi:10.1021/nl102122x
26. Beard MC, Luther JM, Semonin OE, Nozik AJ. Third generation photovoltaics based on multiple exciton generation in quantum confined semiconductors. *Acc Chem Res*. 2013;46(6):1252-1260. doi:10.1021/ar3001958
27. Green MA, Bremner SP. Energy conversion approaches and materials for high-efficiency photovoltaics. *Nat Mater*. 2016;16(1):23-34. doi:10.1038/nmat4676
28. Barnham KWJ, Duggan G. A new approach to high-efficiency multi-band-gap solar cells. *J Appl Phys*. 1990;67(7):3490-3493. doi:10.1063/1.345339
29. France RM, Geisz JF, Song T, et al. Triple-junction solar cells with 39.5% terrestrial and 34.2% space efficiency enabled by thick quantum well superlattices. *Joule*. 2022;6(5):1121-1135. doi:10.1016/j.joule.2022.04.024
30. Liang J, Zhang Z, Xue Q, et al. A finely regulated quantum well structure in quasi-2D Ruddlesden–popper perovskite solar cells with efficiency exceeding 20%. *Energ Environ Sci*. 2022;15(1):296-310. doi:10.1039/D1EE01695D
31. Lei Y, Li Y, Lu C, et al. Perovskite superlattices with efficient carrier dynamics. *Nature*. 2022;608(7922):317-323. doi:10.1038/s41586-022-04961-1
32. Meddeb H, Gotz-Kohler M, Osterthun N, Sergeev O, Gehrke K, Vehse M, Agert C. Ultrathin Multiple Quantum Wells Solar Cell Based on Silicon/Germanium Nanostructures. In: *2021 IEEE 48th Photovoltaic Specialists Conference* (PVSC): IEEE; 2021, pp. 975–978.
33. Toprasertpong K, Inoue T, Nakano Y, Sugiyama M. Investigation and modeling of photocurrent collection process in multiple quantum well solar cells. *Sol Energy Mater sol Cells*. 2018;174:146-156. doi:10.1016/j.solmat.2017.08.036
34. Sayed I, Bedair SM. Quantum Well Solar Cells: Principles, Recent Progress, and Potential.
35. Meddeb H, Götz-Köhler M, Flathmann C, Seibt M, Gehrke K, Vehse M. Novel semi-transparent solar cell based on ultrathin multiple Si/Ge quantum wells. *Prog Photovolt*. 2022;31(12):1396-1408. doi:10.1002/pip.3665
36. Götz M, Lengert M, Osterthun N, Gehrke K, Vehse M, Agert C. Switchable photocurrent generation in an ultrathin resonant cavity solar cell. *ACS Photonics*. 2020;7(4):1022-1029. doi:10.1021/acsphotonics.9b01734
37. Gotz-Kohler M, Meddeb H, Gehrke K, Vehse M, Agert C. Ultrathin solar cell with magnesium-based optical switching for window applications. *IEEE J Photovolt*. 2021;11(6):1388-1394. doi:10.1109/JPHOTOV.2021.3110311
38. Götz-Köhler M, Banik U, Meddeb H, et al. Switchable photovoltaic window for on-demand shading and electricity generation. *Solar Energy*. 2022;232:433-443. doi:10.1016/j.solener.2021.12.071
39. Osterthun N, Neugebohrn N, Gehrke K, Vehse M, Agert C. Spectral engineering of ultrathin germanium solar cells for combined photovoltaic and photosynthesis. *Opt Express*. 2021;29(2):938-950. doi:10.1364/OE.412101
40. WTheiss Hardware and software- CODE/Scout. https://www.wtheiss.com/ (Accessed June 2023).
41. Varache R, Leendertz C, Gueunier-Farret ME, Haschke J, Muñoz D, Korte L. Investigation of selective junctions using a newly developed tunnel current model for solar cell applications. *Solar Energy Mater Solar Cells*. 2015;141:14-23. doi:10.1016/j.solmat.2015.05.014
42. Born M, Wolf E. *Principles of optics: electromagnetic theory of propagation, interference and diffraction of light*. 13thed. Cambridge University Press; 2017.
43. Yu N, Genevet P, Kats MA, et al. Light propagation with phase discontinuities: generalized laws of reflection and refraction. *Science (New York, NY)*. 2011;334(6054):333-337. doi:10.1126/science.1210713
44. Lee K-T, Seo S, Guo LJ. High-color-purity subtractive color filters with a wide viewing angle based on Plasmonic perfect absorbers. *Adv Opt Mater*. 2015;3(3):347-352. doi:10.1002/adom.201400533
45. Behaghel B, Tamaki R, Vandamme N, et al. Absorption enhancement through Fabry-Pérot resonant modes in a 430 nm thick InGaAs/GaAsP multiple quantum wells solar cell. *Appl Phys Lett*. 2015;106(8):81107. doi:10.1063/1.4913469
46. Lee K-T, Lee JY, Seo S, Guo LJ. Colored ultrathin hybrid photovoltaics with high quantum efficiency. *Light Sci Appl*. 2014;3(10):e215-e215. doi:10.1038/lsa.2014.96
47. Yang Z, Ji C, Liu D, Guo LJ. Enhancing the purity of reflective structural colors with ultrathin bilayer media as effective ideal absorbers. *Adv Optical Mater*. 2019;7(21):1900739. doi:10.1002/adom.201900739
48. Lee JY, Lee K-T, Seo S, Guo LJ. Decorative power generating panels creating angle insensitive transmissive colors. *Sci Rep*. 2014;4(1):4192. doi:10.1038/srep04192
49. Yang L, Abeles B. Quantum shift of the optical absorption edge in ultrathin amorphous hydrogenated germanium. *Appl Phys Lett*. 1987;51(4):264-266. doi:10.1063/1.98468
50. Wronski CR, Persans PD, Abeles B. Electrical transport in amorphous hydrogenated Ge/Si superlattices. *Appl Phys Lett*. 1986;49(10):569-571. doi:10.1063/1.97098
51. Goh ESM, Chen TP, Sun CQ, Liu YC. Thickness effect on the band gap and optical properties of germanium thin films. *J Appl Phys*. 2010;107(2):24305. doi:10.1063/1.3291103
52. Liu P, Longo P, Zaslavsky A, Pacifici D. Optical bandgap of single- and multi-layered amorphous germanium ultra-thin films. *J Appl Phys*. 2016;119(1):14304. doi:10.1063/1.4939296
53. Raciti R, Bahariqushchi R, Summonte C, Aydinli A, Terrasi A, Mirabella S. Optical bandgap of semiconductor nanostructures: Methods for experimental data analysis. *J Appl Phys*. 2017;121(23):234304. doi:10.1063/1.4986436
54. Abou-Ras D, Kirchartz T, Rau U. *Advanced characterization techniques for thin film solar cells*. 1sted. Wiley-VCH-Verl; 2011. doi:10.1002/9783527636280
55. Sandberg OJ, Armin A. On the effect of surface recombination in thin film solar cells, light emitting diodes and photodetectors. *Synth Met*. 2019;254:114-121. doi:10.1016/j.synthmet.2019.06.008
56. Breitenstein O, Bauer J, Lotnyk A, Wagner J-M. Defect induced non-ideal dark – characteristics of solar cells. *Superlattices Microstruct*. 2009;45(4–5):182-189. doi:10.1016/j.spmi.2008.10.025

57. Okada Y, Seki S, Takeda T, Kawabe M. Control of dark currents in multi-quantum well solar cells fabricated by atomic H-assisted molecular beam epitaxy. *J Cryst Growth*. 2002;237-239:1515-1518. doi:10.1016/S0022-0248(01)02373-9
58. Rubinelli FA. Simulation of forward dark current voltage characteristics of tandem solar cells. *Thin Solid Films*. 2012;520(13):4449-4454. doi:10.1016/j.tsf.2012.02.053
59. Nelson J, Ballard I, Barnham K, Connolly JP, Roberts JS, Pate M. Effect of quantum well location on single quantum well p-i-n photodiode dark currents. *J Appl Phys*. 1999;86(10):5898-5905. doi:10.1063/1.371609
60. Kempa K, Naughton MJ, Ren ZF, et al. Hot electron effect in nanoscopically thin photovoltaic junctions. *Appl Phys Lett*. 95(23):233121.
61. Würfel P, Würfel U. *Physics of solar cells: from basic principles to advanced concepts*. 3rded. Wiley-VCH; 2016.
62. Wurfel U, Cuevas A, Wurfel P. Charge carrier separation in solar cells. *IEEE J Photovoltaics*. 2015;5(1):461-469. doi:10.1109/JPHOTOV.2014.2363550
63. Wronski CR, Tiedje T, Persans P, Abeles B, Hicks M. Charge transfer enhancement of photoconductivity in hydrogenated amorphous Ge/Si multilayer films. *Appl Phys Lett*. 1986;49(20):1378-1380. doi:10.1063/1.97330
64. Ramey SM, Khoie R. Modeling of multiple-quantum-well solar cells including capture, escape, and recombination of photoexcited carriers in quantum wells. *IEEE Trans Electron Dev*. 2003;50(5):1179-1188. doi:10.1109/TED.2003.813475
65. Meddeb H, Bearda T, Dimassi W, et al. Ultra high amorphous silicon passivation quality of crystalline silicon surface using in-situ post-deposition treatments. *Phys Status Solidi RRL*. 2015;9(1):53-56. doi:10.1002/pssr.201409494
66. Lopez-Garcia AJ, Voz C, Asensi JM, Puigdollers J, Izquierdo-Roca V, Pérez-Rodríguez A. Ultrathin a-Si:H/oxide transparent solar cells exhibiting UV-blue selective-like absorption. *Sol RRL*. 2023;7(7):2200928. doi:10.1002/solr.202200928
67. Toprasertpong K, Delamarre A, Nakano Y, Guillemoles J-F, Sugiyama M. Generalized reciprocity relations in solar cells with voltage-dependent carrier collection: application to p - i - n junction devices. *Phys Rev Appl*. 2019;11(2):024029. doi:10.1103/PhysRevApplied.11.024029
68. Fujii H, Toprasertpong K, Watanabe K, Sugiyama M, Nakano Y. Evaluation of carrier collection efficiency in multiple quantum well solar cells. *IEEE J Photovoltaics*. 2014;4(1):237-243. doi:10.1109/JPHOTOV.2013.2287994
69. Toprasertpong K, Kasamatsu N, Fujii H, et al. Carrier time-of-flight measurement using a probe structure for direct evaluation of carrier transport in multiple quantum well solar cells. *IEEE J Photovolt*. 2014;4(6):1518-1525. doi:10.1109/JPHOTOV.2014.2354256
70. Aeberhard U. Spectral properties of photogenerated carriers in quantum well solar cells. *Solar Energy Mater Solar Cells*. 2010;94(11):1897-1902. doi:10.1016/j.solmat.2010.06.020
71. Aeberhard U. Photovoltaics at the mesoscale: insights from quantum-kinetic simulation. *J Phys D Appl Phys*. 2018;51(32):323002. doi:10.1088/1361-6463/aacf74
72. Aeberhard U. Quantum transport simulation of hot carrier photocurrent generation in quantum well solar cells. *Semicond Sci Technol*. 2019;34(9):94002. doi:10.1088/1361-6641/ab312d
73. Aeberhard U. Simulation of ultrathin solar cells beyond the limits of the Semiclassical bulk picture. *IEEE J Photovoltaics*. 2016;6(3):654-660. doi:10.1109/JPHOTOV.2016.2528405
74. Aeberhard U. Nonequilibrium Green's function picture of nonradiative recombination of the Shockley-read-hall type. *Phys Rev B*. 2019;99(12):125302. doi:10.1103/PhysRevB.99.125302
75. Aeberhard U, Morf RH. Microscopic nonequilibrium theory of quantum well solar cells. *Phys Rev B*. 2008;77(12):125343. doi:10.1103/PhysRevB.77.125343
76. Toprasertpong K, Goodnick SM, Nakano Y, Sugiyama M. Effective mobility for sequential carrier transport in multiple quantum well structures. *Phys Rev B*. 2017;96(7):075441. doi:10.1103/PhysRevB.96.075441
77. Fox M, Ispasoiu R. Quantum Wells, Superlattices, and Band-Gap Engineering. In: Kasap S, Capper P, eds. *Springer handbook of electronic and photonic materials*. Springer International Publishing; 2017:1. doi:10.1007/978-3-319-48933-9_40
78. Sandberg OJ, Sundqvist A, Nyman M, Österbacka R. Relating charge transport, contact properties, and recombination to open-circuit voltage in Sandwich-type thin-film solar cells. *Phys Rev Appl*. 2016;5(4):44005. doi:10.1103/PhysRevApplied.5.044005
79. Nelson J, Paxman M, Barnham KWJ, Roberts JS, Button C. Steady-state carrier escape from single quantum wells. *IEEE J Quantum Electron*. 1993;29(6):1460-1468. doi:10.1109/3.234396
80. Steenhoff V, Juilfs M, Ravekes R-E, et al. Optimized optical field profile in resonant-cavity-enhanced a-Ge:H Nanoabsorber solar cells for tandem cell application. *IEEE J Photovoltaics*. 2017;7(1):3-10. doi:10.1109/JPHOTOV.2016.2617039
81. Yang Y, Yoon G, Park S, et al. Revealing structural disorder in hydrogenated amorphous silicon for a low-loss photonic platform at visible frequencies. *Adv Mater*. 2021;33(9):e2005893. doi:10.1002/adma.202005893
82. Kim S, Patel M, Nguyen TT, Kumar N, Bhatnagar P, Kim J. Highly transparent bidirectional transparent photovoltaics for on-site power generators. *ACS Appl Mater Interfaces*. 2022;14(1):706-716. doi:10.1021/acsami.1c18473
83. Kim S, Patel M, Nguyen TT, Yi J, Wong C-P, Kim J. Si-embedded metal oxide transparent solar cells. *Nano Energy*. 2020;77:105090. doi:10.1016/j.nanoen.2020.105090
84. Osterthun N, Meddeb H, Berends D, et al. Titanium-oxide-based electron-selective contact for ultrathin germanium quantum well solar cell. *Physica Status Solidi (a)*. 2022;219(21):2200292. doi:10.1002/pssa.202200292
85. Lopez-Garcia AJ, Blazquez O, Voz C, Puigdollers J, Izquierdo-Roca V, Pérez-Rodríguez A. Ultrathin wide-bandgap a-Si:H-based solar cells for transparent photovoltaic applications. *Sol RRL*. 2022;6(1):2100909. doi:10.1002/solr.202100909

SUPPORTING INFORMATION

Additional supporting information can be found online in the Supporting Information section at the end of this article.

How to cite this article: Meddeb H, Gehrke K, Vehse M. Optical design and bandgap engineering in ultrathin multiple quantum well solar cell featuring photonic nanocavity. *Prog Photovolt Res Appl*. 2024;1-14. doi:10.1002/pip.3802